This project was funded by grants from the National Science Foundation (PCM 74-18676) and from the National Institutes of Health (GM 20102, RR 00757 and a career development award (STF) GM 70-140-3).

References

ABRAHAMSSON, S. (1972). *Acta Cryst.* A**28**, S248.
ARNDT, U. & AMBROSE, B. K. (1968). *IEEE Trans. Nucl. Sci.* **NS15:N63**, 92–94.
BUERGER, M. J. (1960). *Crystal-Structure Analysis*. New York: John Wiley.
CHARPAK, G. (1970). *Ann. Rev. Nucl. Sci.* **20**, 195–253.
CORK, C., FEHR, D., HAMLIN, R., VERNON, W., XUONG, N. H. & PEREZ-MENDEZ, V. (1973). *Proceedings of the Int. Conf. on Computers in Chemical Education, Ljubljana-Zagreb.*
CORK, C., FEHR, D., HAMLIN, R., VERNON, W., XUONG, N. H. & PEREZ-MENDEZ, V. (1974) *J. Appl. Cryst.* **7**, 319–323.
CORK, C., HAMLIN, R., VERNON, W., XUONG, NG H. & PEREZ-MENDEZ, V. (1975). *Acta Cryst.* A**31**, 702–703.
HASHIZUMA, H., KOHZA, K. & KINOSHITA, K. (1972). *Acta Cryst.* A**28**, S249.
MATTHEWS, D., ALDEN, R. A., BOLIN, J. T., FREER, S. T., HAMLIN, R., XUONG, N., KRAUT, J., POE, M., WILLIAMS, M. & HOOGSTEEN, K. (1977). *Science*, **197**, 452–455.
MINOR, T. C., MILCH, J. R. & REYNOLDS, G. T. (1974). *J. Appl. Cryst.* **7**, 323–333.
PHILLIPS, D. C. (1954). *Acta Cryst.* **7**, 746–751.
TAKANO, T., TRUS, B. T., MANDEL, N., MANDEL, G., KALLAI, O. B., SWANSON, R. & DICKERSON, R. E. (1977). *J. Biol. Chem.* **252**, 759–775.
XUONG, NG. H. & VERNON, W. (1972). ACA Meeting, Albuquerque, Abstract J10.

Acta Cryst. (1974). A**34**, 296–308

Investigation of Thin MoO_3 Crystals by Convergent-Beam Electron Diffraction

BY L. A. BURSILL*, W. C. T. DOWELL, P. GOODMAN & N. TATE

Division of Chemical Physics, CSIRO, PO Box 160, *Clayton, Victoria, Australia* 3168

(*Received* 11 *July* 1977; *accepted* 19 *October* 1977)

The MoO_3 structure is analysed by means of multi-slice calculations for crystals up to 80 Å thick. It is shown that for such thin crystals convergent-beam patterns can be simply analysed. This allows crystal thickness to be readily determined and opens up the way to more precise structure factor measurements. Many-beam calculations are also used to analyse unit-cell and symmetry data obtained by convergent-beam diffraction/microscopy observations of '101' domains in molybdenum trioxide, showing that $[MoO_6]$ octahedra in domains are more nearly regular than in MoO_3. This is supported by analysis of thermal diffuse scattering. The '101' domain structure has space group *Cmcm* and unit-cell parameters identical to those of the molybdenum oxide–hydroxide $Mo_4O_{10}(OH)_2$. A qualitative comparison of calculated and observed intensities for the space-group-forbidden 100 reflexions of MoO_3 indicates the presence of epitaxically deposited surface layers. This observation, together with the evidence of a hydroxylated domain structure, suggests that thin crystals are formed with epitaxic hydroxyl layers which diffuse into the bulk structure when the crystals are heated.

Introduction

Platelet crystals of MoO_3 were formed by burning Mo in air and subsequently collecting the oxide on a thin carbon film. These crystals offer almost ideal test specimens for thin-crystal convergent-beam diffraction. The initial aim of the present investigation was to show which parameters can be conveniently or accurately measured from crystals of only a few unit cells thick. This work could subsequently be continued with a view to obtaining accurate structure factors, since initial calculations have shown thin-crystal data to be relatively free of absorption effects. Work presented here is restricted to making use of the initial and less accurate data, which may nevertheless be usefully interpreted by means of *N*-beam calculations.

Three types of diffraction pattern are used:

(1) Focused convergent-beam diffraction patterns obtained with the source focused on the crystal and giving patterns characteristic of one region. The same patterns in over-exposure allow observation of the thermal-diffuse-scattering (TDS) pattern.

(2) Defocused convergent-beam patterns obtained with the source focused below the crystal. These give

* Permanent address: Department of Physics, Melbourne University, Parkville, Australia.

multi-domain diffraction patterns in which diffraction data from neighbouring regions of the crystal can be compared.

(3) Patterns in which the source is focused on the photographic plate. These patterns, which come from relatively large specimen areas, correspond roughly to normal selected-area diffraction patterns, and offer the best means for observing the structural-diffuse scattering.

Experimental results were obtained from an early version of a modified Siemens Elmiskop (Dowell & Williams, 1976) operating without a crystal goniometer. Suitable patterns were therefore obtained by seeking crystals lying fortuitously close to the [010] zone-axis setting. Some of the patterns used are consequently mis-set from this zone axis, but have been used as examples, either because of the general shortage of data [as for example Fig. 7(*a*)], or because the tilt from the zone axis serves to emphasize a point [as in Fig. 11(*a*)]. Since we have, for simplicity, only made calculations for the exact zone-axis setting, we cannot interpret mis-set patterns with any accuracy. Our ability to obtain any absolute or relative intensity data from these patterns depends upon the very steep thickness dependence and slow angular dependence of intensities from thin crystals. The most we can claim is that reflexions with diffraction vectors perpendicular to the accidental tilt axis (*i.e.* those most affected) will have their intensities increased and decreased along a smooth curve, such that the stronger and weaker members respectively of a reflexion and its conjugate will give upper and lower limits to the zone-axis value. Furthermore, those reflexions with diffraction vectors parallel to this axis will be only slightly affected.

Our presentation relies very much on visual inspection and comparison of patterns. Apart from the problem of mis-setting, this is complicated by a variation of exposure times. It is therefore helpful to note that in experimental patterns the halation around the central beam gives a clue to exposure, and that we can classify exposures into four classes, as light, medium, heavy and overexposure. For example, Figs. 6(*b*), 8, 7(*c*) and 11(*b*) from approximately the same crystal thickness fit into this sequence of categories, and hence present differing photographic characters.

Exposures were timed by hand operation of the shutter in synchronization with a metronome, a technique which was shown to yield accuracies of about 2% for all periods >1 s (and 5–8% for the 1 s period).

In § I we present calculations and details of procedure including thickness determination; § II gives a physical analysis of MoO_3-domain formation in which changes in unit-cell dimension and space group are determined, and § III gives a chemical interpretation of this data. § IV gives the summarized conclusions of the paper.

I. Elementary matching of diffraction patterns and *N*-beam calculations

1. *Precise thickness and crystal-boundary determination*

(*a*) *Layer identity and sequence*

The multi-slice calculation for dynamic intensities allows layer sequence and surface-layer identity to be investigated conveniently, provided slices are chosen to correspond to a structural layer. MoO_3 crystals can be considered as consisting of approximately planar atomic layers of MoO_2 with the sequence

$$MoO_2{-}O_2 \quad MoO_2{-}MoO_2{-}O_2{-}MoO_2. \qquad (1)$$

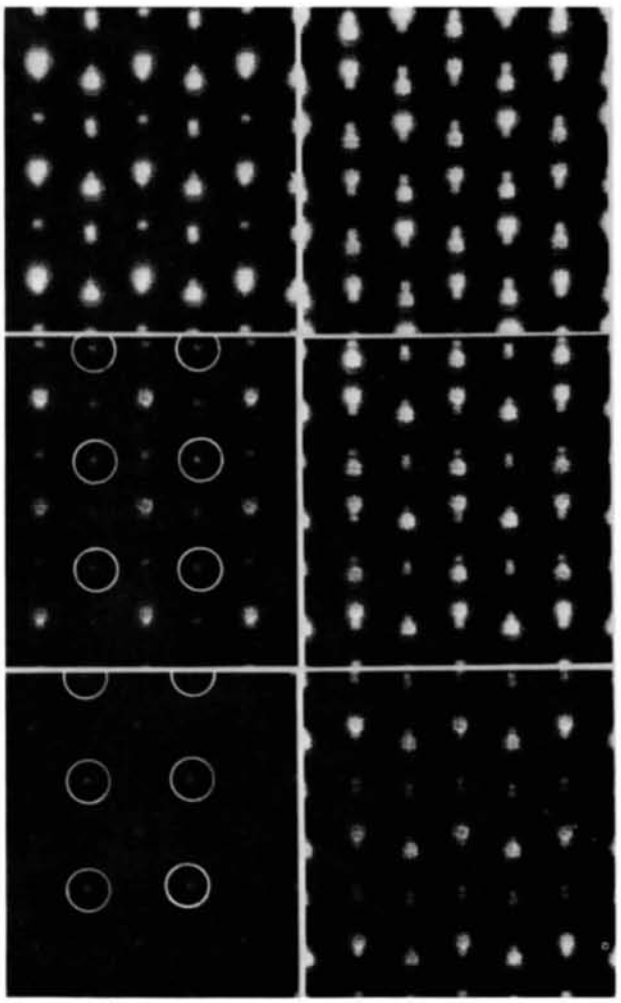

Fig. 1. Half-tone prints, taken by means of the Billington & Kay half-tone process, showing the incremental accumulation of potential as a unit cell is built up from six atomic layers. The sequence runs vertically, from bottom to top, in each column, so that the first frame, corresponding to an atomic layer of oxygen atoms, is at the bottom left, a completed half unit cell is at the top left and a completed unit cell is at the top right. In the first two frames, the oxygen atoms which are foreign to the double-octahedral unit are encircled ('active surface sites' in the text).

This six-layer sequence corresponds to a centrosymmetric unit cell belonging to space group *Pbnm*; a perspective drawing of this cell appears, for example, in Wyckoff (1964). However, this sequence gives no clue to interatomic bonding. The chemically coherent unit of the structure is a double-octahedral layer formed by two mutually bonded sheets of corner-linked MoO_6 octahedra, with a chemical composition in terms of atomic layers of $O{-}MoO_2{-}MoO_2{-}O$. A repeat distance perpendicular to the layers corresponding to the unit-cell dimension of $b = 13{\cdot}94$ Å includes two double-octahedral layers related by a twofold screw axis. Rewriting sequence (1) as

$$O_2{-}MoO_2{-}MoO_2{-}O_2{-}MoO_2{-}MoO_2 \qquad (2)$$

gives a chemically viable repeat unit for use in multi-slice calculations (with one layer per slice) while retaining the six-atomic-layer description. However, it fails to distinguish the two oxygen atoms which, while approximately coplanar and representing atomic sites in the bulk structure, actually belong to separate structural units (*i.e.* separate double-octahedral layers). This becomes a problem only when considering the crystal surface layers, when we wish to carry out the calculation for both the possibilities of occupied and unoccupied extra surface sites. To achieve this flexibility in calculation, we need an eight-atomic-layer description,

$$O{-}MoO_2{-}MoO_2{-}O{-}O{-}MoO_2{-}MoO_2{-}O, \quad (3)$$

for the repeat unit.

The build-up of a unit cell by the successive addition of six layers, following the sequence (2), is shown in Fig. 1, which is a presentation by a computer half-tone process (Billington & Kay, 1974) of the projected potential distribution. This sequence clearly shows the increasing density and changing projected symmetry in progressing through the unit cell. In the first frame of Fig. 1, the two oxygen atoms discussed above are distinguishable. Those atom sites which are not part of the octahedral structural unit in this particular unit cell, but are occupied in the bulk crystal, are shown encircled. In the case of a real crystal surface, these would be 'active' sites with a possible atomic (or molecular) occupation.

(*b*) *Determination of real unit cell*

The first problem to be examined was that of crystal termination. If crystal surfaces could be formed by a single octahedral layer [lowest layer in Fig. 2(*a*)] and the crystal constructed from repeat units given by sequence (1) in the previous section, the space-group-forbidden reflexions 001 and 100 would appear together for certain crystal thicknesses. On the other hand, for crystals bounded by double-octahedral units [upper layer in Fig. 2(*a*)], the 100 reflexion would appear alone for crystals composed of an odd number of such layers. This can be understood by studying a three-dimensional model of the structure, and is displayed in the intensity-*versus*-thickness plots obtained by the six-atomic-layer-slice calculations for the two models already published (Fig. 1, Goodman & Moodie, 1974). In practice, it is found that the 100 reflexion is present or absent with about equal probability in the [010] zone-axis patterns taken, whereas the 001 reflexion never appears in the convergent-beam patterns taken from good crystal regions. This observation is consistent with the crystals being built up from integral double-octahedral layers, depicted in Fig. 2(*b*) and described by sequence (3) in the previous section. The 001 reflexion appears only in patterns from damaged or bent crystal regions.

(*c*) *Thickness determination*

169-beam multi-slice calculations were made using the eight slices per unit cell according to the sequence (3) in § I.1(*a*). Fig. 3 shows intensity-*versus*-thickness curves for five of the zone reflexions. Points corresponding to layer-by-layer increase are shown labelled with the layer type. These points allow us to understand the intensity oscillations of each reflexion in some detail. Since crystal termination can only occur after an integral number of half-unit cells, as described in § I.1(*b*), a stepped curve is also drawn to give observable reflexion intensities corresponding to allowable crystal thicknesses within the range of the plot. One can recognize two distinct types of behaviour: the steady stepwise increase of intensity with thickness shown by the space-group-allowed reflexions (200, 101, *etc.*) and the square-wave oscillation of intensity shown by the space-group-forbidden reflexions 100 and 201.

The behaviour of the space-group-forbidden reflexions revealed by the multi-slice calculations can also be understood kinematically from the progressive projections for quarter, half, and one unit cell shown in Fig. 1. More specifically Fig. 4 shows larger areas for half and one unit cell with the relevant planes labelled. This behaviour is summarized in Table 1.

The classification of Table 1 is also useful in interpreting the TDS and strain-induced diffuse-scattering patterns shown in Figs. 8 and 9.

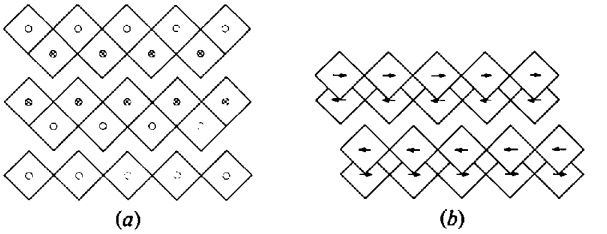

(*a*) (*b*)

Fig. 2. Schematic views of the MoO_3 structure viewed (*a*) along the *a* axis and (*b*) along the *c* axis.

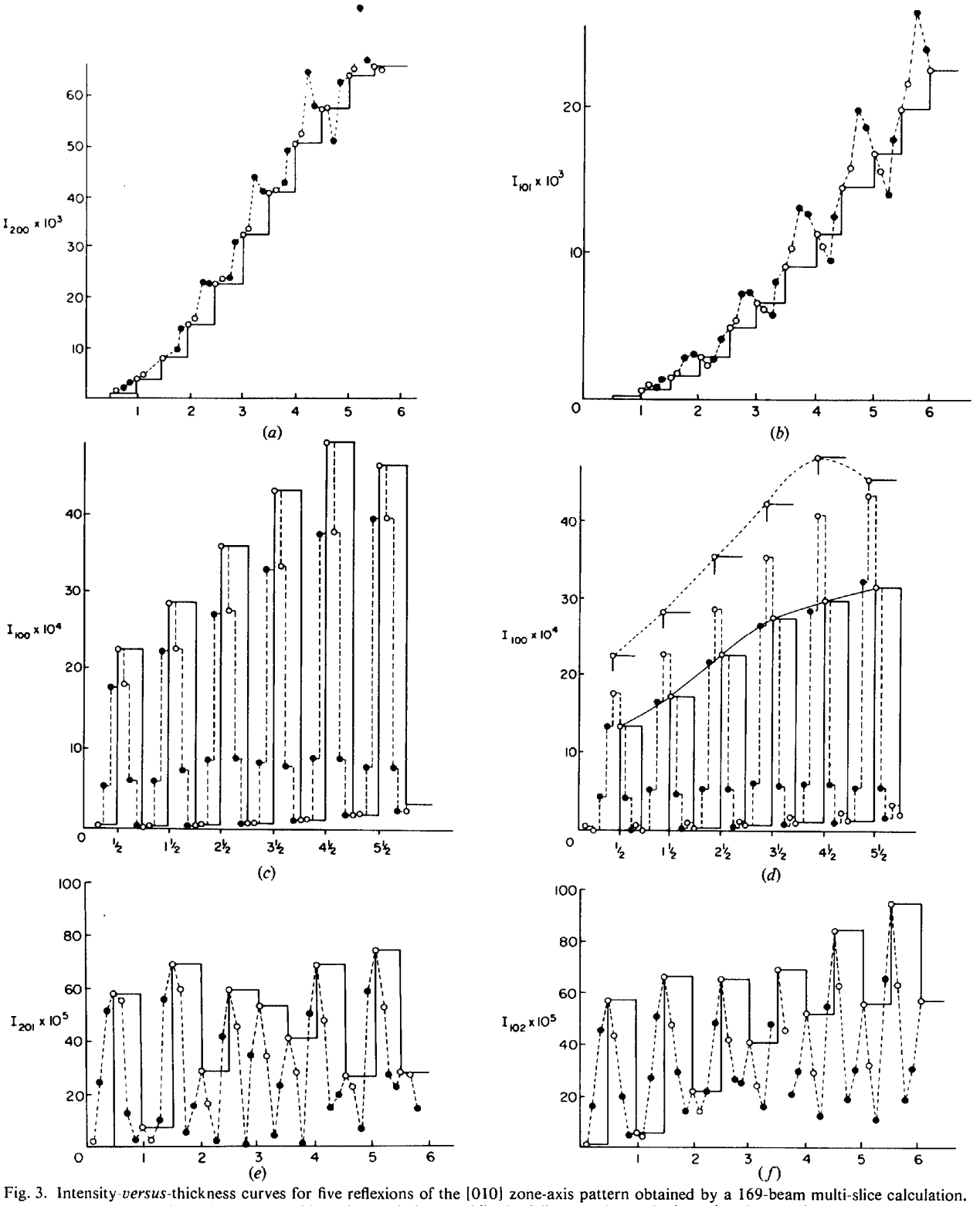

Fig. 3. Intensity-*versus*-thickness curves for five reflexions of the [010] zone-axis pattern obtained by a 169-beam multi-slice calculation. Broken curve shows intensity change with each atomic layer, while the full curve shows the intensity change after each structural unit and hence shows the intensities at chemically allowable thicknesses. The two types of atomic layer are indicated by a full circle for a MoO_2 layer and an unfilled circle for an O-atom layer. Plotted intensities are (*a*) 200, (*b*) 101, (*c*) 100, (*d*) 100 (filled surface oxygen sites), (*e*) 201, and (*f*) 102. In (*d*) curves are shown for both the cases of empty surface sites (partial upper curve with dashed line) and oxygen-filled surface sites (lower curve with full line).

Classification on the basis of dipole dependence (column 4) is furthermore useful in interpreting domain contrast and the influence of thermal vibrations. This classification and the distinction between the 201 and 102 sets of planes can be understood by reference to the projected potentials in Fig. 4. For the present purpose, we note that, dynamically, the 201 reflexion oscillates with thickness but remains weak, while the 100 reflexion, which also oscillates with the same unit-cell periodicity, reaches significant intensities at $(n + \frac{1}{2})$ unit-cell thicknesses.

Calculated results were also displayed as simulated patterns using a seven-level intensity scale and corresponding photographic grey levels. Computed patterns for thicknesses from one unit cell to $3\frac{1}{2}$ unit cells are shown in Fig. 5. The steady increase of pattern intensity with thickness and alternate appearance of the 100 reflexion are clearly shown. This presentation together with numerical values for some of the main reflexion intensity ratios allows a ready thickness identification from the convergent-beam patterns.

Measurements of the intensity ratios I_{200}/I_{000}, I_{002}/I_{000} and I_{202}/I_{000} were obtained by taking patterns with 1, 5, 10 and either 20 or 50 s exposures, and comparing the photographic densities from appropriate exposures. This comparison was aided by a stepped-exposure calibration of the emulsion, and gave intensity ratios to about 5% for the strong reflexions of the zone. However, accuracy of interpretation is restricted in the present instance by deviations of settings from the [010] zone axis: see earlier note.

By comparing the measured and calculated values for any of I_{002}/I_{000}, I_{200}/I_{000} or I_{202}/I_{000}, and noting the presence or absence of the 100 and $\bar{1}00$ reflexions, it was possible to determine the crystal thickness in terms of the precise number of half-unit-cell layers. This simple determination is applicable to crystals whose thickness does not exceed a certain limit, in this case ~80 Å, the value at which the intensity of the main reflexions begins to decrease with thickness. Crystals too thick for this simple analysis can be recognized from the characteristic appearance of intensity modulation within the convergent-beam discs.

Fig. 6(*a*) shows a micrograph of a crystal field in which two crystals are identified as being of one- and three-unit-cell thicknesses, respectively. The one-unit-cell crystal was found to be too thin for further study; the scattering volume of crystal within the focused beam is so small that an exposure time of 50 s was required to obtain the photograph shown in Fig. 6(*c*). After such an exposure, the region showed image contrast like that expected from a region which had partly melted and re-solidified. This region is just visible in Fig. 6(*a*). Correspondingly, the diffraction discs are somewhat diffuse. However, it is noted that this crystal showed no other contrast either before or after irradiation, unlike

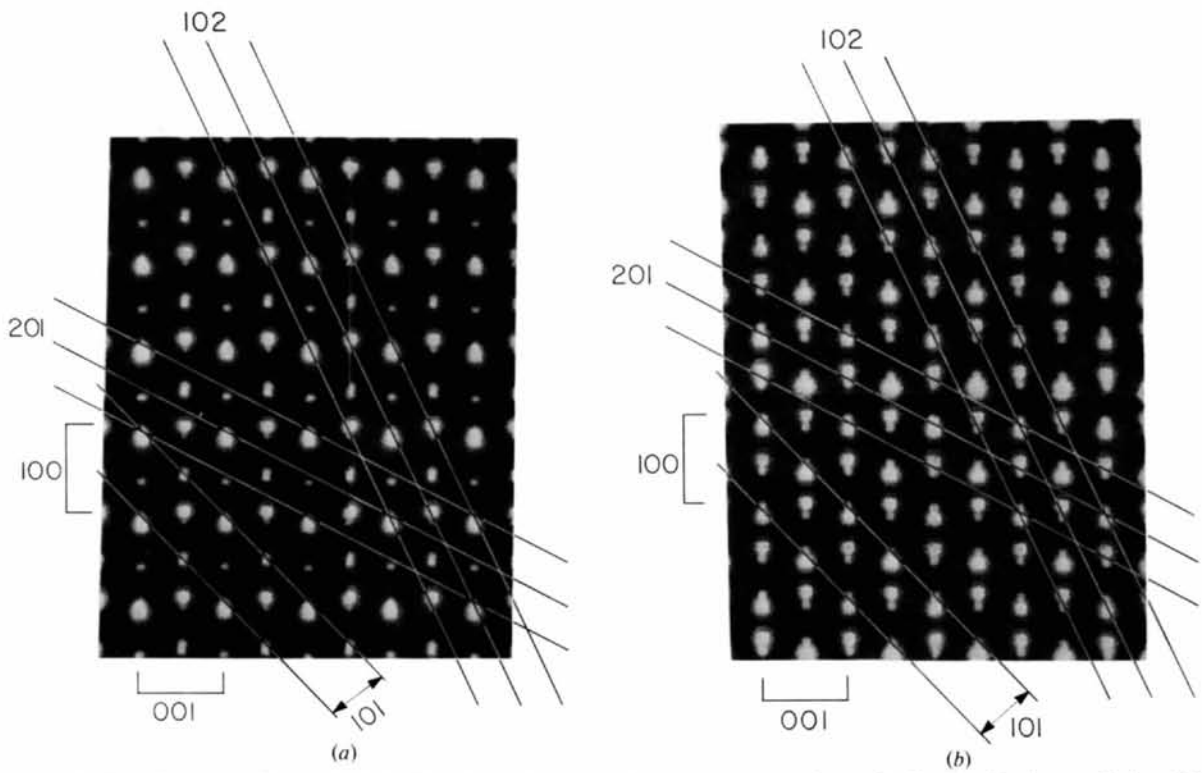

Fig. 4. Projections for one half (*a*) and whole (*b*) unit cell (corresponding to the two top frames in Fig. 1) with planes of index {101}, {201} and {102} drawn in. The 100 and 001 spacings are indicated by square brackets.

Table 1. *Listing of space-group-forbidden reflexions, and the allowed* 101 *reflexion, together with their structural origin, and their dipole dependence*

p denotes reflexions that are kinematically permitted by the fractional unit-cell depth indicated at the head of the column. Reflexions specified as dipole-dependent are those which would be kinematically *absent* for a non-polar structure ('ideal' structure – see text) at the greatest unit-cell depth tabulated as *p* (half unit cell for the 201, one unit cell for the 101).

	h k l	Slice thickness			
		¼ unit cell	½ unit cell	Dipole dependence	1 unit cell
Space-group forbidden	0 0 1	*p*	–	–	–
	1 0 0		*p*	–	–
	2 0 1		*p*	yes	–
	1 0 2		*p*	–	–
Allowed	1 0 1		*p*	yes	*p*

the behaviour of thicker crystals in the electron beam. The three-unit-cell crystal gave a sharp pattern within a practical exposure time, as shown in Fig. 6(*b*), and it was concluded that the thickness range of 3–5½ unit cells was a useful one for structure analysis.

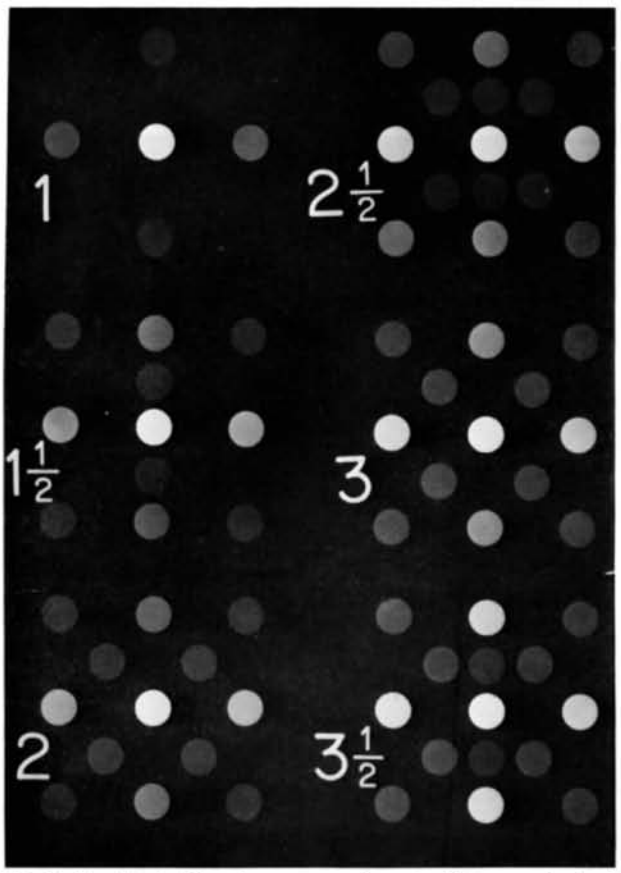

Fig. 5. Simulated diffraction patterns from the *N*-beam calculated results for the [010] zone-axis setting, showing the general increase of diffracted intensity, and alternate appearance of the 100 reflexion, as crystal thickness increases from one unit cell (upper left-hand frame) in half-unit-cell steps, to three-and-a-half unit cells (lower right-hand frame). The patterns are constructed from a seven-level grey scale.

2. *Qualitative comparison of predicted and observed* 101 *and* 100 *intensities*

Unlike the other main reflexions of the zone, the 101 and 100 reflexions show appreciable variation from their predicted intensity values and so cannot be used in a thickness determination based on absolute values.

(*a*) 101 *reflexion*

The 101 reflexion is dependent for its appearance on the dipole character of the structure ('dipole dependence' characteristic of Table 1). Its absence is characteristic of '101' domains (Bursill, 1969). We will henceforth call these regions 'domains' and the remain-

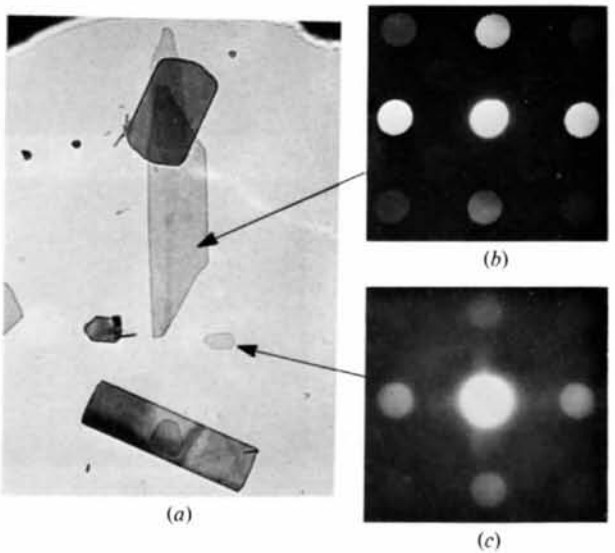

Fig. 6. (*a*) Micrograph showing field of MoO_3 crystals on a carbon supporting film taken with an underfocused convergent beam. Two thin crystals, arrowed, are identified by means of their diffraction patterns of known exposure time, shown in (*b*) and (*c*), as being of three unit cells and one unit cell thickness respectively. The smaller, one-unit-cell, crystal shows two beam-damage spots in the original print, which indicate buckling rather than decomposition at the points from which diffraction patterns were taken.

der of the crystal 'matrix'. The primary observation is that the matrix material gives a finite 101 intensity. However, the more detailed observation is that the 101 intensity is frequently much weakened in patterns from crystals showing a well-developed domain structure. In fact, the relative strength of the 101 reflexion appears to be a fair indication of the degree of domain penetration into a particular microcrystal region. A depression in I_{101} may be readily detected by eye, by observing the relative 101/202 intensities. For example, in Fig. 6(*b*), taken from a crystal exhibiting a large domain structure, the ratio I_{101}/I_{202} should be 0·8 whereas the observed value is nearer 0·3 [compare the pattern of Fig. 6(*b*) with the appropriate calculated pattern of Fig. 5]. In another case (Fig. 7*a*), a relatively good crystal having a thickness of $5\frac{1}{2}$ unit cells gave a pattern which, although slightly mis-set, shows a far better agreement for I_{101}/I_{202}; here, the 101 reflexion has between two and three times the intensity of the 202 reflexion, as in the calculation.

It is interesting to consider the hypothesis that domain growth occurs on a layer-by-layer basis, so that near a domain wall, but within the matrix, some layers have already been transformed to the domain structure. Fig. 8, which is a defocused convergent-beam image of a domain structure, shows that in most regions of the 101-disc image, we can clearly distinguish between the matrix and the domain, since the light regions are sharply defined. However, there are two regions where the domain and matrix coexist. These are shown in the strong 200 and $\bar{2}0\bar{2}$ images respectively, at places indicated by arrows, where one obtains a double image as a result of the two *d* spacings (this is discussed in § II). This results in an intensity level of approximately half the normal level at the corresponding points in the 101 images. These regions are indicated again by arrows (101 reflexion) and a bracket ($\bar{2}0\bar{2}$ reflexion) in the enlarged section shown in Fig. 9. The regions at these points must be of similar composition to that at the focal point for the pattern of Fig. 6(*b*), but their direct observation in a micrograph gives some credence to the domain-growth hypothesis.

(*b*) 100 *reflexion*

The 100 reflexion appears as a sharp disc in diffraction patterns from crystals of non-integral unit-cell thicknesses of both the matrix and 101-domain

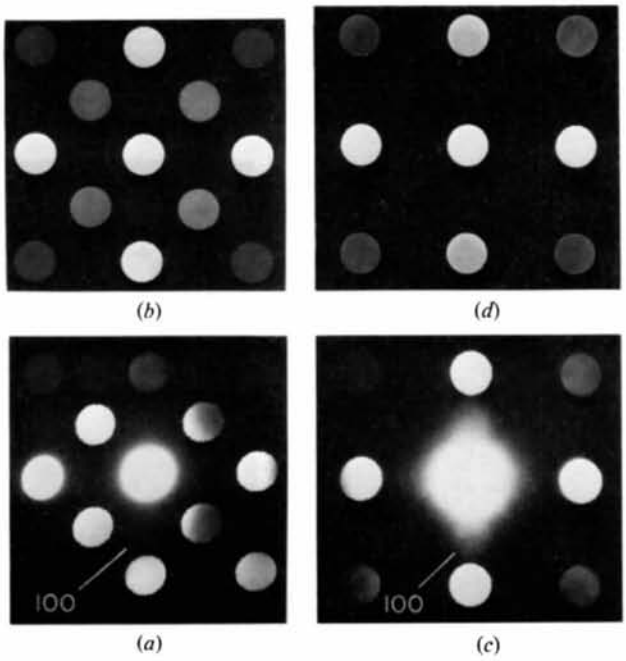

Fig. 7. A comparison of observed and calculated diffraction patterns for two structures. (*a*) Pattern from matrix material having the standard MoO_3 structure and an estimated crystal thickness of $5\frac{1}{2}$ unit cells. (*b*) Computer-derived simulated pattern for the same structure and thickness. (*c*) Pattern from domain material of estimated $3\frac{1}{2}$ unit cells thickness. (*d*) Computer-derived simulated pattern assuming a growth fault (see text). In (*a*) comparison with the calculated pattern is made more difficult by an error in setting corresponding to a rotation from the zone, the rotation occurring about an axis which is nearly parallel (inclined by a few degrees) to the $[100]^*$ vector.

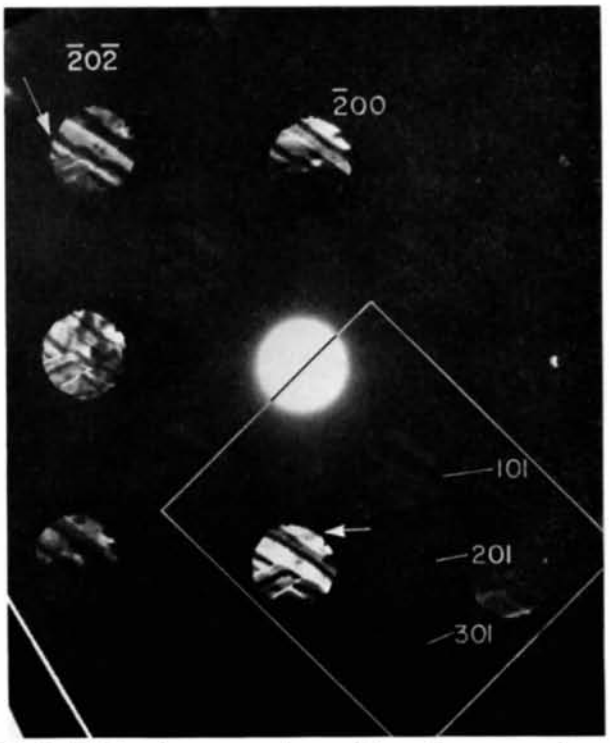

Fig. 8. 101-domain contrast in a defocused convergent-beam pattern at the [010] zone-axis setting. Domain contrast is observed to be in phase in the 101, 201, and 301 reflexions. White and dark overlap regions, indicated in the 200 and 002 reflexions, arise from a unit-cell disparity between matrix and domain material. Micro-regions of coexisting phases, showing a diffraction shift, are indicated by arrows.

material, indicating that the layer constitution of both materials is basically similar. As with the 101 reflexion, its relative intensity level is variable. In some patterns, such as that of Fig. 7(*a*) with approximately normal 101 intensity, the 100 intensity is approximately half that predicted. [Calculated I_{100}/I_{101} ratio is 0·25 at $5\frac{1}{2}$ unit cells; this ratio is simulated in Fig. 7(*b*).] Another example is given in Fig. 9, a defocused domain pattern from a crystal of $3\frac{1}{2}$ unit cells thickness. For this thickness, the I_{100}/I_{101} ratio should be 0·5, whereas the observed level is less than 0·25 (*except* at the region of the domain wall where lattice strain increases the 100 intensity). To summarize, while the 101 intensity varies from a normal value downwards, the 100 intensity, as judged from these few observations, varies from approximately half the normal value downwards and, furthermore, is in some cases considerably diffused, as in Fig. 7(*c*).

The 100 reflexion is strongly influenced by the crystal surface composition. If the active surface sites were filled with oxygen atoms, instead of being empty as assumed in our main calculations, we would start our atomic-layer sequence accordingly, *i.e.* O–O–MoO_2–MoO_2– ..., and obtain the intensity-*versus*-thickness plot of Fig. 3(*d*). In this figure, the stepped intensity curve is drawn so as to give values for crystals following the sequence O–O–MoO_2–MoO_2– ... MoO_2–O–O, *i.e.* corresponding to both surfaces having extra oxygen atoms. The upper-level curve has been transferred from an equivalent calculated result obtained for $(n + \frac{1}{2})$ unit cells without these extra oxygen atoms. Comparing this with the lower continuous line in the figure shows that the extra epitaxically placed oxygen has the effect of reducing the 100 intensity by about 40% at a thickness of $4\frac{1}{2}$ unit cells and 35% at $5\frac{1}{2}$ unit cells. The addition of this extra oxygen layer does not appreciably affect other reflexions of the zone. This calculated result gives a strong indication that the active surface sites on the MoO_3 crystals are indeed often filled, if not with oxygen atoms, then with some heavier species since the reduction in 100 intensity given by these test calculations, although in the right direction, is insufficient to explain all of the results. The present observations are insufficient in number and precision to warrant any more detailed analysis.

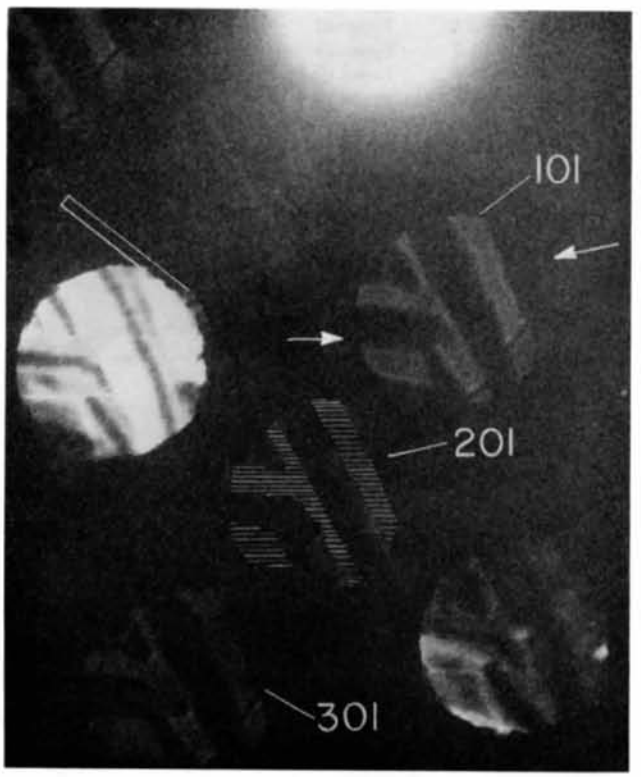

Fig. 9. Enlargement of detail from Fig. 8 in which white domain areas, which might otherwise have been lost in reproduction; have been hatched in the 201 reflexion. A diffraction shift at the edge of the 200 reflexion is indicated. This shift also leads to the black and white interdomain boundaries, and allows the unit-cell discrepancy to be calculated. Arrows to the 101 disc indicate weak-intensity areas discussed in the text.

3. *Calculated results for various hypothetical stacking faults in thin crystals*

Two mechanisms have been suggested as possible explanations for the appearance of 101 domains in MoO_3 crystals. These are (i) a disordering of Mo positions (polar disorder) and (ii) an ordered structure with central Mo positions, corresponding to the 'disordered' and 'ideal' models respectively of Bursill (1969). If a model for polar disorder were determined, it would then be possible to calculate diffracted intensities for various amounts of disorder and hence be in a position to distinguish between the two mechanisms. A question arises as to the energy difference between the regular stacking sequence for MoO_3, in which the Mo polarity alternates in direction from one half-unit-cell layer to the next [as demanded by the twofold screw axis – see Fig. 10(*a*)], and an alternative stacking sequence in which the polarity is unchanged between layers [see Fig. 10(*b*)]. If the energy difference

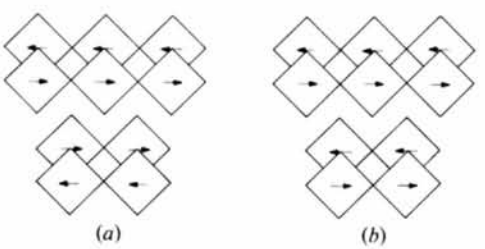

Fig. 10. View of MoO_3 along the *c* axis (*a*) for normal stacking sequence, denoted by '1' in Table 2, and (*b*) for alternative stacking sequence, denoted by '2' in Table 2.

is not too great, then stacking faults with the alternative sequence of Fig. 10(*b*) should occasionally occur. Furthermore, since the bonding within each double-octahedral layer is covalent, stacking faulting of this type is the only reasonable way in which polar disorder could be introduced over an appreciable area. With only van der Waals forces operating between layers, this faulting could occur, while the addition of electrostatic quadrupolar forces will tend to favour one sequence rather than the other.

Two types of polar stacking fault were considered in our calculations: (i) growth faults and (ii) thermal faults. Type (i) fault is a reversal of polarity of all layers past the fault, and from its nature could only occur during crystal growth. Type (ii) fault is a polarity reversal of a *single* layer (and therefore involves two neighbouring stacking faults), which could conceivably result from thermal vibrations. Multi-slice calculations were run for both these hypothetical fault types, and results for a four-unit-cell crystal are shown in Table 2. Introducing a type (i) fault somewhere near the centre of the crystal produces a dramatic reduction of the 101 intensity and, in fact, gives a satisfactory explanation of single-domain patterns such as shown in Fig. 7(*d*). However, these faults correspondingly cause a slight increase in the very weak 201 reflexions. The reason for this can be seen in the intensity-*versus*-thickness curves for the normal and faulted structures. With the normal scattering sequence, the 201 reflexion is almost completely cancelled with a unit-cell periodicity, whereas the 101 reflexion is reinforced [see Fig. 3(*b*), (*e*)]. With the alternative stacking sequence of the fault structure, the reverse is true: the 201 reflexion is built up at the expense of the 101 reflexion.

A type (ii) fault acts to reduce the 101 reflexion intensity, but certainly the reduction is not sufficient to explain the observed 101-domain diffraction pattern. Furthermore, these faults cause a significant increase in 201 intensity, to a level comparable to the reduced 101 intensity (see Table 2). Finally, calculations were run showing the result of varying densities of both types of fault occurring in the one crystal. These show a combination of the above effects.

These results can henceforth be used in analysis of the domain structure in thin crystals.

Table 2. *Influence of polar stacking faults on* 101 *and* 201 *intensities for a four-unit-cell crystal*

Stacking sequence*	Structure	Reflexion strength as a percentage of I_{002} 101	201
1 1 1 1 1 1 1 1	Normal	11	0·5
1 1 1 2 1 1 1 1	Type (i)	2	0·6
1 1 1 1 2 1 1 1	Type (i)	1·5	0·7
1 1 1 1 1 2 2 1	Type (ii)	6	1·3
1 1 1 1 2 2 1 1	Type (ii)	6	4·5
1 2 1 2 1 1 1 1	Types (i) & (ii)	3	1·4
1 2 1 2 1 2 2 1	Types (i) & (ii)	0·7	1·3

* 1 = normal sequence; 2 = alternate sequence.

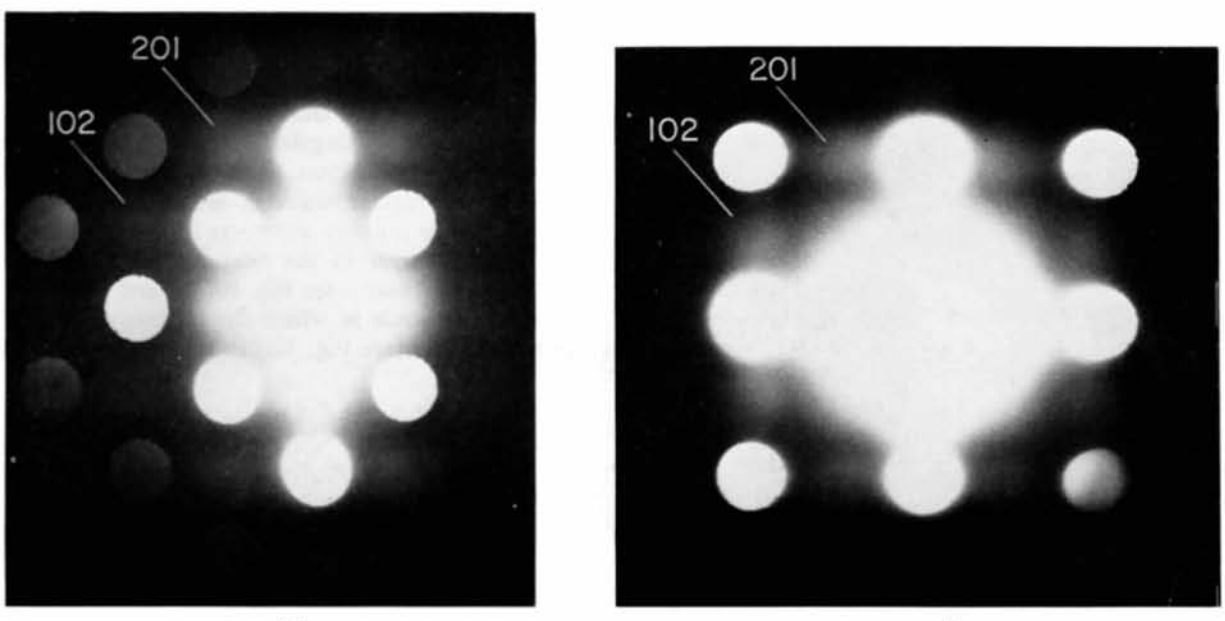

(*a*) (*b*)

Fig. 11. Over-exposures of focused convergent-beam diffraction patterns taken close to the [010] zone-axis setting, showing the characteristic TDS distribution (*a*) from the MoO_3 matrix material, and (*b*) from a 101-domain. Both patterns show a strong 100–001 cross through the origin. (*b*) shows approximate symmetry between the 201/102 TDS peaks, which is absent in (*a*).

II. Evidence for the nature of the domain structure

1. *Use of multi-domain patterns*

Initial experiments showed us that not enough information could be obtained from single-domain convergent-beam patterns, taken at exact convergent-beam focus, to determine the origin of the 101 domains: both models (i) and (ii) above could be made to give a sufficiently good explanation of the patterns to our present accuracy. However, more detailed patterns showing domain contrast could be obtained by slightly defocusing the convergent beam. Initial observations showed that domain contrast existed in crystals freshly deposited on a substrate and maintained at approximately 200°C, prior to electron-beam irradiation. This was shown by moving non-irradiated crystals quickly through the electron beam. A multi-domain pattern showing satisfactory spatial resolution was obtained and shown in Fig. 8. Examination of detail in this pattern shows that the disorder model (i) cannot be the correct one for the explanation of domain formation. If this mechanism *were* the correct one, domain contrast in 201 reflexions would be opposite to that in the 101 reflexions (*i.e.* the bright regions in one would correspond to dark regions in the other). The 201 and 101 domains are actually parallel in contrast (see Fig. 9), and this observation supports the hypothesis (ii) of a centred structure described by Bursill as 'ideal' (Fig. 23, Bursill, 1969). (The origin of detectable 201 contrast at a thickness of about three unit cells can be found in Fig. 3, which shows that at this thickness the initial one-unit-cell oscillation has changed phase for the 201 reflexion, resulting in a detectable intensity.) The detectability of weak domain contrast on top of considerable TDS in the case of the 201 reflexion (which appears clearly in the over-exposure of Fig. 11) is apparently due to the ability of the eye to differentiate the sharp domain features in the presence of background.

Closer examination of Fig. 8 shows that the lattice parameters of the domain structure differ slightly from those of the non-domain or standard structure. This can be seen from relative image shifts. On the inside edge of the 200 reflexion, where there is a small matrix region inside the 101-domain [see § I.2(*a*)], an increase of reciprocal lattice spacing of about 3% can be observed, indicated by an arrow in Fig. 8 and a bracket in Fig. 9, corresponding to a contraction of the *a* parameter of the unit cell within the domain structure. This relative shift of domain image outwards from the central beam also causes a reduction of intensity at the inner domain boundaries and an intensity enhancement at the outer boundaries, as shown in Fig. 9. An explanation of these image shifts in terms of a tilt between domain and non-domain regions of the crystal is ruled out here because of the large relative tilts required, and also because in this case the relative shifts would be in the opposite direction to that observed. Similarly, a smaller outward shift of the disc edge in the c^* direction in the $20\bar{2}$ reflexion at a second small 'co-existence' zone, together with intensity enhancement of 'inner' and reduction of 'outer'-domain edges in the $00\bar{2}$ reflexion disc, indicates a relative contraction of the 101-domain *c* dimension by about 1%.

This evidence is compatible with the hypothesis that the 101-domain material is chemically distinct from the matrix, and this point is taken up in detail in § III.

2. *Thermal diffuse scattering*

The TDS distribution can be obtained by over-exposure of a focused convergent-beam pattern. Over-exposures of the zone-axis pattern from the MoO_3 matrix (Fig. 11*a*) and from a 101 domain (Fig. 11*b*) show the same essential features, namely: (i) two strong streaks running from the origin and passing through the 100 and 001 positions respectively, and (ii) less intense but definite streaks running through the 200 and 002 positions and displaced from the origin. These streaks can be readily understood from vibrations of the Mo atoms along the [001]* and [100]* directions of their oxygen octahedra.

In order to obtain a qualitative understanding of the distributions, the assumption can be made that vibrations *within* each double-octahedral layer are independent of those occurring in neighbouring layers. However, coupling between neighbouring Mo atoms within a structural layer can occur as a result of electrostatic and covalent forces. Thus, motion of a Mo atom along the 100 or polar diagonal of the MoO_3 structure will tend to induce parallel movement of neighbouring Mo atoms within the same single-octahedral (quarter-unit-cell) layer (covalent coupling), and anti-parallel movement of Mo atoms in the other single-octahedral layer with which it is bonded by octahedral edge sharing (electrostatic coupling). Similar considerations will apply to motion along the [001] diagonal direction. However, in the former case ([100] direction), a complication arises in the MoO_3 structure in that this is the polar direction, so that the Mo atoms sit in off-central positions in an asymmetric potential well. A strong anharmonic component of vibrations is therefore to be expected for vibrations in this direction. This component would be expected to reduce the 101 structure factor and introduce a TDS peak at the 201 positions. The same component would not, however, contribute to the peaks at 102 positions (see Fig. 5 and Table 1).

Thus, 201/102 TDS asymmetry is a predictable consequence of the structural polarization. This asymmetry is, in fact, a feature of TDS patterns from the matrix MoO_3 (Fig. 11*a*), but not of those from the domain material (Fig. 11*b*), which maintains a fairly clear fourfold symmetry. This latter observation is

regarded as further evidence supporting the non-polar or 'ideal' interpretation for the domain structure (see conclusions in § IV). The 101 position is a trough in the TDS pattern from MoO_3, between the 201, 100 and 001 peaks; this trough is also predictable from a coupled anharmonic component of vibration along the 100 direction.

The other more obvious and simpler features of the TDS patterns, mainly the intense streaks from the origin through the 100 and 001 positions, can be understood as being due to Mo atom vibrations along these principal directions with limited and varying degrees of coupling within the single octahedral layer.

3. *Structural diffuse scattering*

When diffraction patterns are taken from larger areas of a single crystal, by defocusing the objective lens and focusing the electron beam on the observation screen using the second condenser lens, patterns similar to those obtained by the conventional selected-area technique are obtained. When an MoO_3 crystal which has been irradiated for several minutes by the electron beam is used, the zone-axis pattern shown in Fig. 12 is obtained. This pattern, which is similar to patterns obtained (though not interpreted in detail) by Bursill (1969), shows well-developed disorder-diffuse scattering with a clearly defined distribution. Both the 100 and 001 positions show both sharp and associated diffuse peaks. These peaks arise from the combination of a radiation-damaged structure with the averaging over a range of crystal orientations in the beam. Measurement of the separation between the 100 reflexion and its diffuse satellite gives a value of approximately $6d_{100}$ for the 'superlattice' spacing. The satellite separation is roughly constant for all diffraction orders. Two types of diffuse distribution are associated with the reciprocal lattice points. These are (1) asymmetrical distributions about the 100, 201 and other reflexions, and (2) symmetrical distributions about 001, 200 and other reflexions. The first clue to an interpretation comes from recognizing that the asymmetric distributions are associated with single-layer reflexions (column 3 of Table 1), and that the symmetric distributions (with the notable exception of that associated with the 001 position) are associated with double-layer reflexions (column 5 of table 1). With this classification, the pattern can be recognized in outline as arising from a periodic strain structure which is set up independently in one or more structural layers.

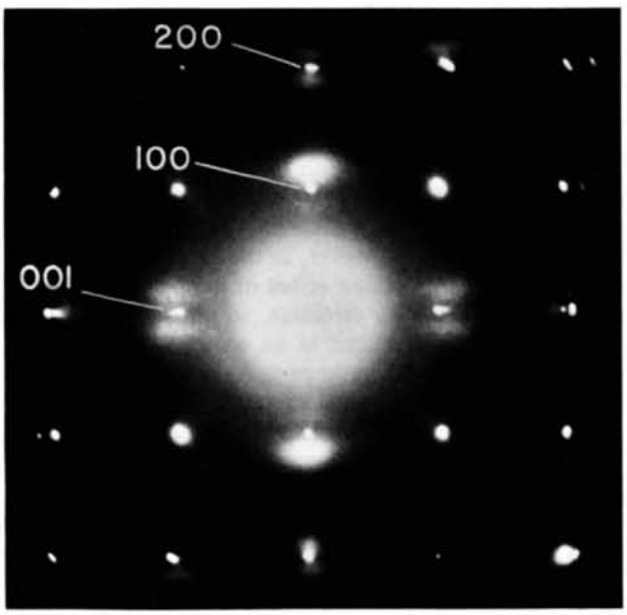

Fig. 12. Selected-area-type diffraction pattern from a large region of a single crystal taken by focusing the beam by means of the second condenser lens onto the recording photographic plate. Both asymmetric and symmetric disorder-diffuse peaks are clearly seen.

An analysis in more detail is as follows. The asymmetric peak outside the 100 reflexion is consistent with a periodic compression of the 100 planes occurring more or less independently in each double-octahedral layer of the structure. The 200 reflexion then has a symmetrical diffuse distribution, since it is essentially a two-layer reflexion (*i.e.* the 200 intensity from a single layer is small, and it is reinforced by the second half of the unit cell). Thus, a distorted layer will beat against an undistorted second layer to give equal contributions to compression and expansion lattice modulations. The symmetrical 001 peaks are also understood from this model, when we further recognize that the double-octahedral layers are themselves composed of fairly rigid chains of edge-sharing octahedra running parallel to the (001) planes. Thus, the (001) planes are periodically bent in either direction, as a result of displacements parallel to 100. Finally, there is a very weak diffuse peak on the inside of the 002 reflexions, indicating to some extent a stretching of the [001]-directed chains, but this peak is also much weaker than the 100 peak.

The above description is simply a geometric interpretation of the diffuse pattern. With regard to the structural origins of the strain field, the following evidence has to be taken into account:

Table 3. *Comparison of all parameters, space-group and extinction conditions for* MoO_3 *and* $Mo_4O_{10}(OH)_2$

Structure	Cell dimensions (Å)	Space group	Extinction conditions
MoO_3	$a = 3{\cdot}9628$ $b = 13{\cdot}855$ $c = 3{\cdot}6964$	*Pbnm*	$0kl, k + l = 2n + 1$ $h0l, l = 2n + 1$
$Mo_4O_{10}(OH)_2$	$a = 3{\cdot}888$ $b = 14{\cdot}082$ $c = 3{\cdot}634$	*Cmcm*	$hkl, h + k = 2n + 1$ $h0l, l = 2n + 1$

(1) The diffuse pattern appears in the wide-area (*i.e.* selected-area) diffraction pattern from crystals after several minutes of beam irradiation.

(2) Defocused convergent-beam patterns (not shown here) taken from domain areas giving diffuse patterns show that the diffuse intensity arises mainly from the MoO_3 matrix rather than from the domains. This, indeed, is consistent with the appearance of definite asymmetric 201 peaks, which would be absent in the case of a domain origin (see Table 3).

(3) Dark-field images (Bursill, 1969) (Fig. 8) show the appearance within the matrix of line contrast parallel to the domain walls, coincident with the appearance of the diffuse pattern.

(4) Further heat treatment of the material at this stage results in the further growth of the domain structure at the expense of the matrix MoO_3. The process can be repeated until approximately half the material is transformed into domain material. This behaviour suggests that the cycle of radiation damage followed by annealing of domains can be repeated until all the available reactant is consumed.

The most obvious source of structural-diffuse scattering is the strain field associated with the domain boundaries. Strain from a linear intergrowth, which produces the moiré frequency, is out by a factor of about three in predicting the observed 100 satellite spacing. However, since the domain boundaries run at a non-crystallographic direction of about 35° to the [001] direction, it is probable that the microstructure contains steps parallel to the [100] and [001] directions. A plausible model for periodic strain can therefore be proposed, involving an *average* step distance of $6d_{100}$ along the boundaries, as indicated schematically in Fig. 13. In this case, the increase in diffuse-scattered intensity with irradiation can be related to the increasing number of narrow micro-domains, as evidenced by the fine line contrast appearing in the dark-field images.

The development at a later stage of radiation dosage of more complicated streaks and superlattice twins (Bursill, 1969) is a separate phenomenon involving both the domain and matrix material. There are at present insufficient data to extend interpretation to these latter phases. It is noted that the structural-diffuse scattering indicates that domain-wall strain is a single-layer phenomenon; this supports an earlier hypothesis [§I. 2(*a*)] that domain growth occurs on a layer-by-layer basis.

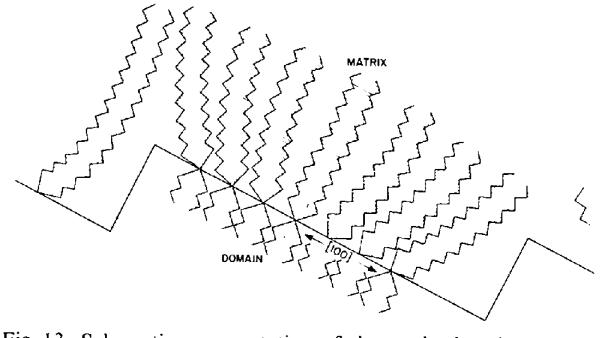

Fig. 13. Schematic representation of the strained region between matrix and domain structures across a stepped 100 boundary, showing lateral compression of the zigzag MoO_3 chains within the matrix at the line of intergrowth.

III. Chemical interpretation of domain formation

The evidence presented here concerning the domain structure supports the hypothesis that the structure is chemically distinct from the MoO_3 matrix, and can be identified with a molybdenum oxide–hydroxide structure of the type $MoO_{3-x}(OH)_x$. Glemser & Lutz (1951) demonstrated the close connection between these reduced hydroxides (x = 0·5, 1·0, 1·6 and 2·0 were reported) and MoO_3 by showing the possibility of stepwise reduction and oxidation. Kihlborg, Hägerström & Ronnquist (1961) used powder X-ray methods to determine the cell parameters and symmetry for $Mo_4O_{10}(OH)_2$ (x = 0·5). Their data for MoO_3 and $Mo_4O_{10}(OH)_2$ are compared in Table 3. They reported that the intensity distribution in the powder patterns of $MoO_{2.5}(OH)_{0.5}$ is remarkably similar to that of MoO_3, with the important exception that all reflexions hkl for which $h + k = 2n + 1$ and $h0l$ for which $l = 2n + 1$ are absent. This indicated a C centring of the lattice with considerably less distortion of the MoO_6 octahedra. The structure of $Mo_4O_{10}(OH)_2$ was determined using single-crystal X-ray diffraction by Wilhelmi (1969) with crystals prepared by hydrothermal synthesis at 25 kbar and 600–1000°C. The structure shows a strong tendency towards a more ideal octahedral configuration with the Mo atoms lying on mirror planes of the structure perpendicular to the a axis.

The H positions were not determined, but it was suggested that the most likely sites are between the double octahedral layers. The relevant bond lengths were consistent with typical hydrogen bonds. Wilhelmi also suggested that the existence of a series of discrete oxide–hydroxide phases $MoO_{3-x}(OH)_x$ (x = 0·5, 1·0, 1·6, and 2·0) makes it very possible that the H atoms in $Mo_4O_{10}(OH)_2$ are ordered in some way. A similar transition to a more ideal octahedral coordination of Mo atoms was found for $MoO_{3-x}F_x$ (Sleight, 1969; Pierce & Vlasse, 1971).

The extinction conditions $h0l$, $h+l = 2n+1$ for $Mo_4O_{10}(OH)_2$ immediately explain the dark-field observations of the domain patterns [Bursill, 1969; Fig. 7(*a*) and (*b*)] and the in-phase nature of the 101 and 201 multi-domain convergent-beam images (Figs. 8 and 9). The observed contraction of a by 3% and expansion of c by 1% is clearly consistent with the difference of cell parameters for MoO_3 and $MoO_4O_{10}(OH)_2$ (~2% and 1% respectively).

It is difficult to estimate the stoichiometry of the domain structure. Our earlier estimate of $x = 2{\cdot}9975$ for MoO_x (Bursill, 1969) was based on the assumption that the domain structure was intimately related to the density of the crystallographic shear planes which form at higher temperatures. It is now clear that, if the domain structure is due simply to hydrogenation of the MoO_3 crystals according to the reaction

$$MoO_3 + \frac{x}{2}H_2 = MoO_{3-x}(OH)_x,$$

then there is no relation between the domain stoichiometry and that of the shear structure formed at higher temperatures. Glemser & Lutz (1951) found only four members of the series $MoO_{3-x}(OH)_x$ having $x = 0{\cdot}5$, $1{\cdot}0$, $1{\cdot}6$ and $2{\cdot}0$, but it is quite possible for smaller x values to occur. If, for a crystal n unit cells thick, we assume that the MoO_3 crystal surfaces absorb a monolayer containing H onto active oxygen sites, we obtain stoichiometry $4nMoO_3 + H_2$, *i.e.* $MoO_{3-x}(OH)_x$ with $x = 1/2n$. Thus, a crystal five unit cells thick (70 Å) would have $x = 0{\cdot}1$. Given that the domains usually occupy only approximately one third of the crystal volume, this corresponds to domain stoichiometry $MoO_{2{\cdot}6}(OH)_{0{\cdot}4}$, which is surprisingly close to $Mo_4O_{10}(OH)_2$. This example shows that the thin crystal surfaces could plausibly be the primary carriers of the reactant, prior to domain formation. We therefore suggest that all our available evidence is consistent with reactant ions containing hydrogen being epitaxically collected on the crystals during specimen preparation, and subsequently diffusing into the structure during the initial heat treatment at 200°C to form domains of a hydroxide nature.

Attempts to prepare single crystals of the domain material have so far been unsuccessful, although macroscopic domains within MoO_3 crystals can be readily prepared [see Fig. 16(*a*) in Bursill, 1969]. These always occur as the minor phase. Wilhelmi also found that MoO_3 and $Mo_4O_{10}(OH)_2$ always occurred together in parallel intergrowth with the obvious topotactic relationship. Further investigation of domain formation must depend upon more detailed microscopy of the domain boundaries. These are nearly parallel to $\{302\}_{MoO_3}$ when the domains are large and well-developed, but taper to lenticular shape at the ends. As yet, we have no explanation for the habit-plane indices. The mechanism of domain growth shows close similarities with spinodal decomposition in the earliest stages, when an ill-defined cross-hatched pattern appears. Later, larger regions of well-defined parallel domains appear, when the process more closely resembles cellular precipitation [*cf.* Figs. 5(*a*) and 7(*a*) in Bursill, 1969].

IV. Conclusions

The present study has established the following points:

(1) It is possible to determine precise crystal thickness and, consequently, to make accurate measurements of structure factors from substances which occur naturally only in the form of thin sheets, as well as from others which may be prepared in that form.

(2) Thin-crystal diffraction analysis can also be a means, in suitable cases, of determining such surface properties as crystal surface-layer composition, and the present or absence of foreign-atom expitaxic layers.

(3) Examples given illustrate the particular advantages of convergent-beam microscopy as opposed to conventional transmission microscopy for certain problems. In particular, the ability to correlate reliably a set of weak- and strong-beam 'dark-field' images can be a valuable aid in analysis of a multi-phase preparation.

(4) Useful TDS patterns can be obtained from overexposures of focused convergent-beam patterns of thin crystals. This is in contradistinction to the requirements of thick and flat perfect crystals previously established for conventional point-pattern diffraction.

(5) The present analysis has resolved the problem of domain formation in MoO_3 crystals by showing that it arises from the local formation of a second structure, measurably different in its unit-cell dimension and space group. All data obtained is consistent with the formation of domains of $Mo_4O_{10}(OH)_2$, by a reaction with hydroxyl ions collected on the crystal during crystal growth, and diffused into the structure by subsequent heat treatment.

The authors wish to acknowledge assistance given in computer programming by Mr A. Wilson and Mr T. Secomb, and to thank Messrs Billington and Kay for programming the computer display of Figs. 1 and 4, and Miss Robin Goodman for the computation and preparation of the simulated diffraction pattern series of Fig. 5 and Fig. 7(*b*) and (*d*).

References

BILLINGTON, C. & KAY, N. R. (1974). *Aust. J. Phys.* **27**, 73–85.

BURSILL, L. A. (1969). *Proc. R. Soc. London*, A**311**, 267–290.

DOWELL, W. C. T. & WILLIAMS, D. (1976). *Ultramicroscopy*, **2**, 43–48.

GLEMSER, O. & LUTZ, G. (1951). *Z. Anorg. Allg. Chem.* **264**, 17–19.

GOODMAN, P. & MOODIE, A. F. (1974). *Acta Cryst.* A**30**, 280–290.

KIHLBORG, L., HÄGERSTRÖM, G. & RONNQUIST, A. (1961). *Acta Chem. Scand.* **15**, 1187.

PIERCE, J. W. & VLASSE, M. (1971). *Acta Cryst.* B**27**, 158–163.

SLEIGHT, A. W. (1969). *Inorg. Chem.* **8**, 1764–1767.

WILHELMI, K.-A. (1969). *Acta Chem. Scand.* **23**, 419–429.

WYCKOFF, R. W. G. (1964). *Crystal Structures*, Vol. 2. New York: John Wiley.